

Fusion of Hyperspectral and LiDAR Data Using Sparse and Low-Rank Component Analysis

Behnood Rasti, *Member, IEEE*, Pedram Ghamisi, *Member, IEEE*,
Javier Plaza, *Senior Member, IEEE*, and Antonio Plaza, *Fellow, IEEE*

Abstract—The availability of diverse data captured over the same region makes it possible to develop multisensor data fusion techniques to further improve the discrimination ability of classifiers. In this paper, a new sparse and low-rank technique is proposed for the fusion of hyperspectral and light detection and ranging (LiDAR)-derived features. The proposed fusion technique consists of two main steps. First, extinction profiles are used to extract spatial and elevation information from hyperspectral and LiDAR data, respectively. Then, the sparse and low-rank technique is utilized to estimate the low-rank fused features from the extracted ones that are eventually used to produce a final classification map. The proposed approach is evaluated over an urban data set captured over Houston, USA, and a rural one captured over Trento, Italy. Experimental results confirm that the proposed fusion technique outperforms the other techniques used in the experiments based on the classification accuracies obtained by random forest and support vector machine classifiers. Moreover, the proposed approach can effectively classify joint LiDAR and hyperspectral data in an ill-posed situation when only a limited number of training samples are available.

Index Terms—Extinction profiles (EPs), feature fusion, hyperspectral, light detection and ranging (LiDAR), sparse and low-rank component analysis (SLRCA).

I. INTRODUCTION

NOWADAYS, diverse remote sensors are available, thus allowing us to obtain complementary information from different sources for materials on the surface of the earth. Such information can vary from spectral information obtained by passive sensors [e.g., multispectral and hyperspectral images (HSIs)], to height and shape information acquired by light detection and ranging (LiDAR) sensors, as well as texture information to amplitude and phase by synthetic aperture radar. The availability of data coming from these multiple sources now allows researchers worldwide to integrate such diverse information to improve object detection ability and classification performance. Regardless of the great amount of

knowledge available in such data sets, automatic interpretation of remote sensed data still remains a challenge [1].

HSIs are capable of defining the phenomenology and the spectral characteristics of different objects over a detailed spectral signature. LiDAR data, instead, can be used to characterize the elevation and object height information of the scene. These two data sets have been intensively investigated for different tasks [2].

Urban scenes are usually highly complex and challenging. It is generally optimistic to assume that a single sensor can provide enough information for classification and feature extraction [3]. To this end, HSIs may not be able to precisely differentiate objects composed of the same material (i.e., objects with the same spectral characteristics). For instance, roofs and roads, which are made by the same material, exhibit the same spectral characteristics [4]. Therefore, it is difficult to differentiate such categories in the feature space. On the other hand, the use of LiDAR elevation data alone cannot discriminate objects with the same elevation but made of different materials (e.g., roofs with the same elevation built by concrete or asphalt). Furthermore, the individual use of LiDAR data for complex areas, e.g., where many classes are located close to each other, is very limited compared with optical data, due to the lack of spectral information provided by this type of sensor [5], [6].

To take advantage of information provided by different sensors, multisensor data fusion can be taken into account. The joint use of HSI and LiDAR has been investigated in several applications, such as shadow-, height-, and gap-related masking techniques [7]–[9], above-ground biomass estimates [10], microclimate modeling [11], quantifying riparian habitat structure [12], and fuel type mapping [13]. Moreover, the joint use of LiDAR and HSI has led to higher discrimination power in the feature space compared with the individual use of each source [1], [14]–[18]. For instance, in [17], the joint investigation of HSI and LiDAR was taken into account for the classification of complex forested areas using only pure spectral information classified by either support vector machines (SVMs) or Gaussian maximum likelihood. In [19], deep convolutional neural network was developed to fuse features extracted from HSI and LiDAR to precisely classify land-cover classes. In [18], graph-based feature fusion and morphological profiles were used to fuse LiDAR-derived features and HSI in a fewer dimensional space. In [20], HSI and LiDAR have been considered to deal with individual tree classification, which could also be extended to areas of shadow caused by the illumination of tree crowns with sunlight. That approach

Manuscript received December 3, 2016; revised April 15, 2017; accepted July 3, 2017. Date of publication August 3, 2017; date of current version October 25, 2017. (Corresponding author: Pedram Ghamisi.)

B. Rasti is with the Keilir Institute of Technology, 235 Reykjanesbaer, Iceland, and also with the Department of Electrical and Computer Engineering, University of Iceland, 107 Reykjavik, Iceland (e-mail: behnood.rasti@hi.is; behnood@Keilir.net).

P. Ghamisi is with the German Aerospace Center, Remote Sensing Technology Institute, 82234 Weßling, Germany, and also with the Signal Processing in Earth Observation, Technische Universität München, 80333 Munich, Germany (e-mail: pedram.ghamisi@dlr.de).

J. Plaza and A. Plaza are with the Hyperspectral Computing Laboratory, Escuela Politécnica de Cáceres, University of Extremadura, 06071 Badajoz, Spain (e-mail: jplaza@unex.es; aplaza@unex.es).

Color versions of one or more of the figures in this paper are available online at <http://ieeexplore.ieee.org>.

Digital Object Identifier 10.1109/TGRS.2017.2726901

was applied to a complex forested area to classify the scene into 16 classes of tree species. In [21], spectral, spatial, and elevation features extracted from HSI and LiDAR were fused via orthogonal total variation component analysis, which is able to estimate the fused features in a lower dimensional space and also promote piecewise smoothness while maintaining the spatial structures. The aforementioned works indicate that LiDAR and HSI can complement each other effectively and that integrating these two sources of information in an appropriate manner, one can make the most of the advantages of the two, while addressing the shortcomings of each of them. However, the automatic integration of multiple types of data is not a trivial task [16]. In addition, spatial information, which plays a key role for the classification of HSI, in particular the ones that are of high spatial resolution, has been neglected in most of the conventional approaches.

In [22], the concept of extinction profiles (EPs) was proposed, and later in [23], the concept of EPs has been generalized to extract spatial and contextual information from HSI. In contrast with attribute profiles (APs) [24]–[26], EPs preserve the height of the extrema kept [22], which leads to a higher simplification for recognition capability. This advantage leads to higher classification accuracy for EPs compared with the results obtained by APs. More importantly, EPs are automatic in nature, and also independent from the kind of the attribute being used (e.g., area, volume, etc.). However, the initialization of threshold values used in APs is difficult and time consuming.

Although the joint use of HSI and LiDAR information can potentially improve classification accuracies, the automatic fusion of such data is not straightforward [16]. Moreover, the simple concatenation of extracted features obtained by different sensors might increase the so-called *curse of dimensionality*, while the number of training samples is limited [25], [27]–[31]. To address this issue, different feature reduction approaches can be taken into account [25]. This encourages to develop an effective and efficient fusion approach to perform both dimensionality reduction and feature fusion simultaneously [18].

Due to the spectral redundancy in HSI, it has been shown that low-rank HSI modeling provides great advantages in HSI analyses, such as denoising [32], unmixing [33], and feature extraction [34]. In [34], HSI low-rank modeling was incorporated with sparse regression called sparse and low-rank component analysis (SLRCA). An SLRCA using wavelet bases given in [35] was shown that HSI can be restored based on a few sparse components.

Hyperspectral and LiDAR data provide valuable information of a scene such as height, spatial, and spectral characteristics. On the one hand, extracting different kinds of information and features is crucial for the classification task. On the other hand, it could decrease the classification accuracy due to the Hughes phenomenon. As a result, in this contribution, we seek for a remedy to the aforementioned dilemma. Therefore, instead of stacking the extracted features, here, we estimate the fused features assumed to live in a lower dimensional space. More specifically, in this paper, a new fusion technique for HSI and LiDAR data is proposed based on the use of SLRCA applied

on the EPs. First, EPs are used to extract spatial and elevation information from HSI and LiDAR, respectively. At the next stage, the HSIs as well as the extracted EPs from HSI and LiDAR are fused based on a sparse and low-rank technique, where the spectral redundancy of the features is captured by the low-rank property, while the sparsity property helps to capture spatial redundancy of the features. The sparsity property promotes the spatial smoothness on the fused features, which leads to a region-wise homogeneous classification map, and the low-rank property of the fusion technique avoids the Hughes phenomenon [27], and therefore, both improve the classification accuracy. The proposed fusion technique is evaluated based on classification accuracies obtained by applying both random forest (RF) and SVM classifiers on the fused features. The performance of the proposed fusion approach is also evaluated in a situation when there is only a limited number of training samples are available.

The rest of this paper is organized as follows. After giving a short description for the notations used in this paper, Section II describes the proposed fusion technique. The experiments are described in Section III. Finally, Section IV concludes this paper with some remarks.

A. Notation

In this paper, the numbers of bands and pixels in each band of the HSI are denoted by p and n , respectively. Matrices are denoted by bold and capital letters, column vectors by bold letters, the element placed in the i th row and j th column of matrix \mathbf{X} by x_{ij} , and the i th column by $\mathbf{x}_{(i)}$. The identity matrix of size $p \times p$ is denoted by \mathbf{I}_p . $\hat{\mathbf{X}}$ stands for the estimate of the variable \mathbf{X} , and \mathbf{X}^m denotes the estimate of the variable \mathbf{X} at the m th iteration. The Frobenius norm and the Kronecker product are denoted by $\|\cdot\|_F$ and \otimes , respectively. The matrix vectorization operator is shown by vec .

II. METHODOLOGY

As can be seen from Algorithm 1, the proposed feature fusion approach is composed of two main phases. In the first phase, EPs are used to extract spatial and elevation features from HSI and LiDAR, respectively. The second phase fuses spectral, spatial, and elevation features using SLRCA. In the following, we elaborate on these two phases.

A. Phase I: Extinction Profiles

Ghamisi *et al.* [22] proposed EPs using a set of extinction filters (EFs), which are connected and able to maintain relevant image extrema. Relevance here is defined with respect to the concept of extinction value, proposed in [36]. The extinction value of a regional extremum (minimum or maximum) of any increasing attribute is the maximal size of the attribute filter [37], such that this extremum still exists after filtering [36].

The definition of the extinction value for a regional maximum given in [36] is as follows. Let M be a regional maximum of a grayscale image \mathbf{X} , and $\Psi = (\psi_\lambda)_\lambda$ represents a family of decreasing connected antiextensive transformations. The extinction value corresponding to M with respect to

Algorithm 1 SLRCA Fusion**Input:****HSI** = Hyperspectral data,**L** = LiDAR data, r : Number of fused features, λ : Regularization tuning parameter, ϵ : Tolerance values.**Output:** $\hat{\mathbf{F}}_{fused}$: Fused features estimated.**Phase I :****H** = *normalized*(**HSI**),**F**_{HSI} = *normalized*(EP(**HSI**)),**F**_{LiDAR} = *normalized*(EP(**L**)),**F** = [**F**_{HSI}, **H**, **F**_{LiDAR}],**Phase II :****Initialization:** \mathbf{V}^0 ,**while** $|J^{(k+1)} - J^{(k)}| \leq \epsilon$ **do****W-step :****S** = $\mathbf{D}^T \mathbf{F} \mathbf{V}^m$,**W** ^{$m+1$} = *Soft*(**S**, λ),**V-step :****W** ^{$m+1$} $\mathbf{D}^T \mathbf{F}$ = $\mathbf{Q} \Sigma \mathbf{G}^T$,**V** ^{$m+1$} = $\mathbf{Q} \mathbf{G}^T$,**end** $\hat{\mathbf{F}}_{fused} = \mathbf{D} \hat{\mathbf{W}}$.

Ψ denoted by $\varepsilon_\Psi(M)$ is the maximal λ value, such that M is still a regional maxima of $\psi_\lambda(\mathbf{X})$. This definition can be shown as follows:

$$\varepsilon_\Psi(M) = \sup\{\lambda \geq 0 | \forall \mu \leq \lambda, M \subset \text{Max}(\psi_\mu(\mathbf{X}))\} \quad (1)$$

where $\text{Max}(\psi_\mu(\mathbf{X}))$ is a set containing all the regional maxima of $\psi_\mu(\mathbf{X})$. In the same manner, extinction values of regional minima can be defined. Extinction values can be efficiently computed on a max-tree structure [38].

EFs are connected filters, which preserve the relevant extrema of the grayscale image \mathbf{X} . This filtering approach are defined as follows. Let $\text{Max}(\mathbf{X}) = \{\mathbf{M}_1, \mathbf{M}_2, \dots, \mathbf{M}_N\}$ be the regional maxima of the grayscale image \mathbf{X} . For the input grayscale image \mathbf{X} , the EF preserves the n maxima with the highest extinction values, $\text{EF}^n(\mathbf{X}) = \mathbf{R}_\mathbf{X}^\delta(\mathbf{G})$, where $\mathbf{R}_\mathbf{X}^\delta(\mathbf{G})$ denotes the reconstruction by dilation [39] of the mask image \mathbf{X} from marker image \mathbf{G} . The marker image can be obtained through $\mathbf{G} = \max_{i=1}^n \{\mathbf{M}'_i\}$, where \max is the pixel-wise maximum operation. \mathbf{M}'_1 is the maximum with the highest extinction value, followed by \mathbf{M}'_2 with the second highest extinction value, and so on. For detailed description, please see [22].

EFs for increasing attributes (e.g., area, height, volume, and diagonal of the bounding box) can be efficiently implemented using the max-tree structure [40]. The use of EFs for nonincreasing attributes (e.g., standard deviation), however, demands the construction of the second tree that takes the image to the space of shapes [41] allowing the creation of a novel class of connected operators from the leveling

family and more complex morphological analysis, such as the computation of extinction values for nonincreasing attributes. For more information, please see [22].

EPs are constructed by applying several EFs, i.e., a sequence of thinning and thickening transformations, with progressively higher threshold values to extract spatial and contextual information of the input data. The EP for the input grayscale image, \mathbf{X} , is obtained by

$$\text{EP}(\mathbf{X}) = \underbrace{\{\phi^{P_{\lambda_s}}(\mathbf{X}), \phi^{P_{\lambda_{s-1}}}(\mathbf{X}), \dots, \phi^{P_{\lambda_1}}(\mathbf{X}), \mathbf{X}\}}_{\text{thickening profile}}, \underbrace{\{\gamma^{P_{\lambda_1}}(\mathbf{X}), \dots, \gamma^{P_{\lambda_{s-1}}}(\mathbf{X}), \gamma^{P_{\lambda_s}}(\mathbf{X})\}}_{\text{thinning profile}} \quad (2)$$

where $P_\lambda : \{P_{\lambda_i}\} (i = 1, \dots, s)$ is a set of s ordered predicates (i.e., $P_{\lambda_i} \subseteq P_{\lambda_k}, i \leq k$). It should be noted that the number of extrema is considered as the predicates. ϕ and γ are thickening and thinning transformations, respectively.

EPs can be of any type. In this context, multi-EPs (MEPs) concatenate several types of EPs (e.g., area, height, volume, diagonal of bounding box, and standard deviation) as a single stacked vector, which is defined as follows:

$$\text{MEP}(\mathbf{X}) = \{\text{MEP}_{a_1}(\mathbf{X}), \text{MEP}_{a_2}(\mathbf{X}), \dots, \text{MEP}_{a_w}(\mathbf{X})\} \quad (3)$$

where $a_k, k = \{1, \dots, w\}$ represents different types of extinction attributes. Since different extinction attributes provide complementary spatial and contextual information, the MEP has a greater ability in extracting spatial information than a single EP.

The EP (and its extension MEP) described above was introduced to extract spatial and contextual information from grayscale images. In order to make the EP applicable for HSI, one can extract a few informative features from the whole dimensionality using an approach such as independent component analysis (ICA). Then the extracted features are considered as base images to produce EPs [23]. In this way, an extended EP (EEP) can be obtained, which is a generalization of the EPs. More precisely, EEP, first, reduces the dimensionality of the data from $E \subseteq \mathbf{Z}^n$ to $E' \subseteq \mathbf{Z}^m (m \leq n)$ with a generic transformation $\Psi : E \rightarrow E'$ (i.e., ICA). Second, the EP is performed on the most informative features $\mathbf{Q}_i (i = 1, \dots, m)$, which can be defined as

$$\text{EEP}(\mathbf{Q}) = \{\text{EP}(\mathbf{Q}_1), \text{EP}(\mathbf{Q}_2), \dots, \text{EP}(\mathbf{Q}_m)\}. \quad (4)$$

In order to effectively exploit spatial and contextual information from HSIs, different extinction attribute filters $a_k, k = \{1, \dots, w\}$, can be applied to the first informative features of ICA [i.e., $\mathbf{Q}_i (i = 1, \dots, m)$]. In this manner, EMEP can be constructed

$$\text{EMEP}(\mathbf{Q}) = \{\text{MEP}(\mathbf{Q}_1), \text{MEP}(\mathbf{Q}_2), \dots, \text{MEP}(\mathbf{Q}_m)\}. \quad (5)$$

Fig. 1 illustrates a general work flow of the EMEP. For detailed information, please refer [22] and [23]. It is important to note that the EMEP and EP approximately require the same computational time since the most time consuming part is on the construction of the max-tree and min-tree, which are computed only once for each grayscale image [22], [23].

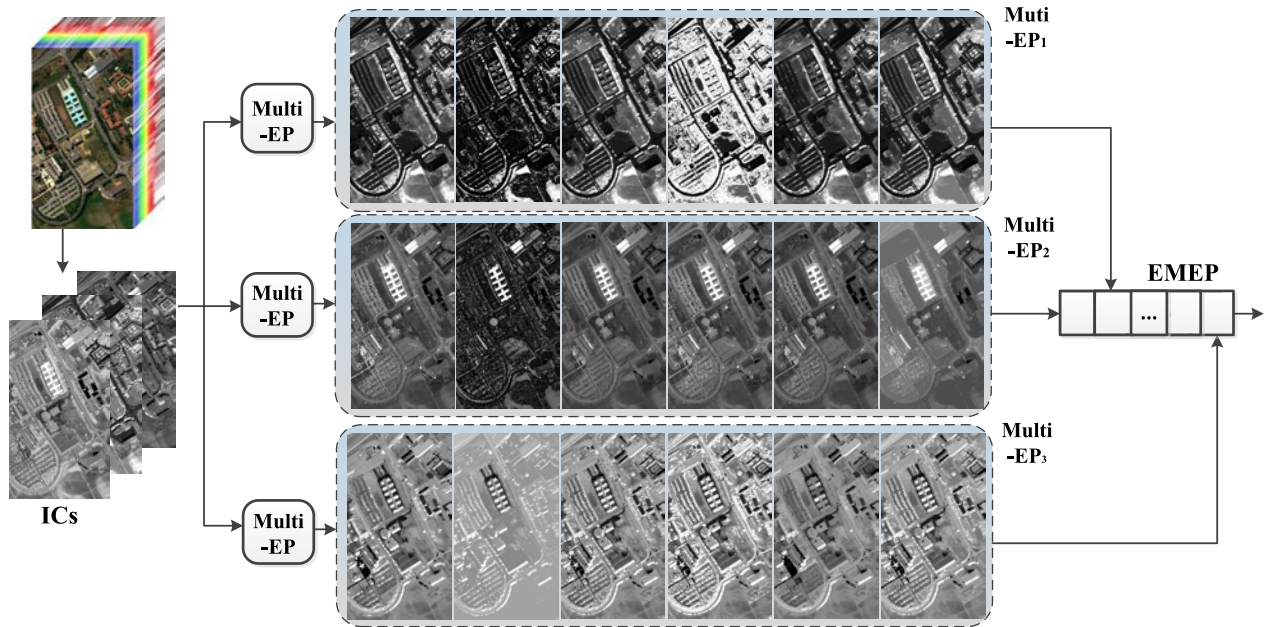


Fig. 1. Simple work flow of the EMEP. First, we preserve only the first three independent components extracted from the whole hyperspectral data cube. Then, each independent component is treated as one base image to produce MEPs including five extinction attributes (i.e., area, volume, standard deviation, diagonal of the bounding box, and height). Finally, all MEPs extracted from three different ICs are concatenated to construct the EMEP.

Since the LiDAR-derived digital surface model (DSM) contains only one component, its corresponding elevation information can be extracted using (3) where \mathbf{X} denotes the LiDAR-derived DSM feature.

EPs extract spatial and contextual information considering the number of extrema, which leads not only to better results in terms of classification accuracies compared with APs but also decreases the burden of setting threshold values, which was a burden for conventional APs [22].

For the sake of simplicity, in the rest of this paper, \mathbf{HSI} denotes the input hyperspectral data (i.e., spectral information), $\mathbf{EP}_{\mathbf{HSI}}$ represents EMEP(\mathbf{Q}) (i.e., spatial information), and $\mathbf{EP}_{\mathbf{LiDAR}}$ demonstrates MEP(\mathbf{X}) (i.e., elevation information).

B. Phase II: Feature Fusion Using Sparse and Low-Rank Component Analysis

To fuse spectral (\mathbf{HSI}), spatial ($\mathbf{EP}_{\mathbf{HSI}}$), and elevation ($\mathbf{EP}_{\mathbf{LiDAR}}$) features, one needs to normalize the number of dimensionalities to put the same weight on each type of the feature and reduce the computational cost and noise throughout the feature space [42]. To do so, kernel principal component analysis [43] was used as an effective tool to reduce the dimensionality of each type of feature independently, since it can represent a higher order complex and nonlinear distribution in a fewer number of dimensions to address Hughes phenomenon [27] and high computational cost. The normalized dimension of \mathbf{HSI} , $\mathbf{EP}_{\mathbf{HSI}}$, and $\mathbf{EP}_{\mathbf{LiDAR}}$ is automatically set to the smallest dimension of the above-mentioned features. For example, for the Houston data, this value is set to 71 [1].

Let \mathbf{H} be the normalized matrix contained the input spectral information (band i is located in column i). $\mathbf{F}_{\mathbf{HSI}}$ represents the normalized spatial features produced by EPs on the first

three independent components (i th feature in its i th column). $\mathbf{F}_{\mathbf{LiDAR}}$ is the normalized elevation features obtained by EPs on the LiDAR derived DSM (i th feature in its i th column).

Extracted features from HSI and LiDAR are highly redundant. In order to reduce the features redundancy, we propose a low-rank model for the fused features. In other words, the extracted features from LiDAR and HSI can be represented in a space of lower dimension. Note that this redundancy of features can affect the classification results due to the Hughes phenomenon [27] and also fused features are expected to have a lower dimension. Hence, we suggest to use the following low-rank model:

$$\mathbf{F} = \mathbf{D}\mathbf{W}\mathbf{V}^T + \mathbf{N} \quad (6)$$

where $\mathbf{F} = [\mathbf{F}_{\mathbf{HSI}}, \mathbf{H}, \mathbf{F}_{\mathbf{LiDAR}}] = [\mathbf{f}_{(i)}]$ is an $n \times p$ matrix containing the i th vectorized feature in its i th column, \mathbf{V} is an unknown subspace (low-rank) basis ($p \times r$), \mathbf{D} is an $n \times n$ orthogonal 2-D wavelet transform matrix, $\mathbf{W} = [\mathbf{w}_{(i)}]$ is an $n \times r$ matrix containing the unknown 2-D wavelet coefficients for the i th component in its i th column, and $\mathbf{N} = [\mathbf{n}_{(i)}]$ is an $n \times p$ matrix containing the vectorized noise and error at band i in its i th column. The purpose of the 2-D wavelet transformation \mathbf{D} is to capture the spatial correlations in the model and the purpose of \mathbf{V} is to capture the low-rank structure of the features. Note that r is the number of fused features ($1 \leq r \leq p$), and p is the total number of extracted features including spectral features. It is worth mentioning that model (6) preserves spatial information of the features (see the Appendix).

In order to estimate the wavelet coefficients \mathbf{W} and the basis matrix \mathbf{V} in (6), we use an SLRCA given in [35], which is based on solving the following nonconvex ℓ_1 penalized least

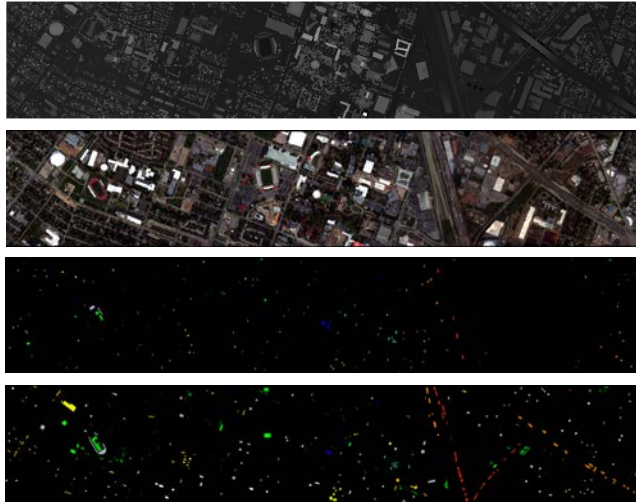


Fig. 2. Houston—from top to bottom: LiDAR-derived rasterized data set, a color composite representation of the HSI using bands 64, 43, and 22 as R, G, and B, respectively, training samples, test samples, and legend of different classes.

squares problem:

$$(\hat{\mathbf{W}}, \hat{\mathbf{V}}) = \arg \min_{\mathbf{W}, \mathbf{V}} J(\mathbf{W}, \mathbf{V}) = \arg \min_{\mathbf{W}, \mathbf{V}} \frac{1}{2} \|\mathbf{F} - \mathbf{D}\mathbf{W}\mathbf{V}^T\|_F^2 + \lambda \sum_{i=1}^r \|\mathbf{w}_{(i)}\|_1 \quad \text{s.t. } \mathbf{V}^T \mathbf{V} = \mathbf{I}_r. \quad (7)$$

The estimated fused features are given by $\hat{\mathbf{F}}_{fused} = \mathbf{D}\hat{\mathbf{W}}$.

C. Estimation

A cyclic descent-type algorithm given in [44] and [35] is used to solve (7) called SLRCA, which solves the nonconvex problem (7) with respect to one variable at a time while the other variable is assumed to be fixed. Therefore, SLRCA consists of the following two steps.

1) *W-Step*: Given a fixed \mathbf{V} , the optimization problem (7) can be rewritten as

$$\arg \min_{\mathbf{W}} \frac{1}{2} \|\mathbf{F} - \mathbf{D}\mathbf{W}\mathbf{V}^T\|_F^2 + \lambda \sum_i \|\mathbf{w}_{(i)}\|_1. \quad (8)$$

Since \mathbf{D} and \mathbf{V} are orthogonal matrices, it can be shown [35] that the minimization problem (8) is equivalent to

$$\arg \min_{\mathbf{W}} \frac{1}{2} \|\mathbf{S} - \mathbf{W}\|_F^2 + \lambda \sum_i \|\mathbf{w}_{(i)}\|_1 \quad (9)$$

where $\mathbf{S} = \mathbf{D}^T \mathbf{F} \mathbf{V}$. It can be shown ([35]) that the solution to this minimization problem is given by

$$\hat{w}_{ji} = \max(0, |s_{ji}| - \lambda) \frac{s_{ji}}{|s_{ji}|}. \quad (10)$$

Function (10) is called soft-thresholding and often is written as

$$\hat{\mathbf{W}} = \text{soft}(\mathbf{S}, \lambda). \quad (11)$$

Note that soft function in (11) is applied element-wise on the matrix \mathbf{S} .

2) *V-Step*: Given a fixed \mathbf{W} , the optimization problem (7) turns to a reduced-rank procrustes problem [45] as

$$\arg \min_{\mathbf{V}} \|\mathbf{F} - \mathbf{D}\mathbf{W}\mathbf{V}^T\|_F^2 \quad \text{s.t. } \mathbf{V}^T \mathbf{V} = \mathbf{I}_r,$$

which has a solution given by $\hat{\mathbf{V}} = \mathbf{Q}\mathbf{G}^T$ where \mathbf{Q} and \mathbf{G} are computed using singular value decomposition of $\mathbf{M} = \mathbf{W}^T \mathbf{D}^T \mathbf{F} = \mathbf{Q}\mathbf{\Sigma}\mathbf{G}^T$. A description of the method is given in Algorithm 1.

III. EXPERIMENTAL RESULTS

A. Data Description

1) *Houston Data*: The data are composed of an HSI and a LiDAR-derived DSM. This data set was distributed for the 2013 GRSS data fusion contest. The hyperspectral data were acquired by the Compact Airborne Spectrographic Imager over the University of Houston campus and the neighboring urban area on June 23, 2012. The LiDAR data were acquired on June 22, 2012. The data sets were collected by the NSF-funded Center for Airborne Laser Mapping. The size of the data is 349×1905 with a spatial resolution of 2.5 m. The hyperspectral data set consists of 144 spectral bands ranging 0.38–1.05 μm . The 15 classes of interests are Grass Healthy, Grass Stressed, Grass Synthetic, Tree, Soil, Water, Residential, Commercial, Road, Highway, Railway, Parking Lot 1, Parking Lot 2, Tennis Court, and Running Track. The ‘‘Parking Lot 1’’ includes parking garages at the ground level and also in elevated areas, while ‘‘Parking Lot 2’’ corresponds to parked vehicles. Fig. 2 shows a false color composite representation of the hyperspectral data and the corresponding training and test samples. Table I gives information about the number of training and test samples for different classes of interests.

It should be noted that we have used the standard sets of training and test samples for the above-mentioned data sets to make the results fully comparable with the available literature.

Cloud shadows in the hyperspectral data were detected using thresholding of illumination distributions calculated by the spectra. Relatively small structures in the thresholded illumination map were removed based on the assumption that cloud shadows are larger than structures on the ground.¹

2) *Trento Data*: The second data set was captured over a rural area in the south of the city of Trento, Italy. The size of the data set is of 600×166 pixels. The LiDAR DSM data were acquired by the Optech ALTM 3100EA sensor and the hyperspectral data captured by the AISA Eagle sensor, all with a spatial resolution of 1 m. The hyperspectral data consist of 63 bands ranging from 402.89 to 989.09 nm, where the spectral resolution is 9.2 nm. The spatial resolution of this data set is 1 m. For this data set, six classes of interests were extracted, including Building, Woods, Apple trees, Roads, Vineyard, and Ground. Fig. 3 shows a false color composite representation of the hyperspectral data and the corresponding training and test samples. Table II gives information about the number of training and test samples for different classes of interests.

¹The enhanced data set was provided by Prof. N. Yokoya from Technical University of Munich.

TABLE I
HOUSTON—NUMBER OF TRAINING AND TEST SAMPLES

Class		Number of Samples	
No	Name	Training	Test
1	Grass Healthy	198	1053
2	Grass Stressed	190	1064
3	Grass Synthetic	192	505
4	Tree	188	1056
5	Soil	186	1056
6	Water	182	143
7	Residential	196	1072
8	Commercial	191	1053
9	Road	193	1059
10	Highway	191	1036
11	Railway	181	1054
12	Parking Lot 1	192	1041
13	Parking Lot 2	184	285
14	Tennis Court	181	247
15	Running Track	187	473
Total		2,832	12,197

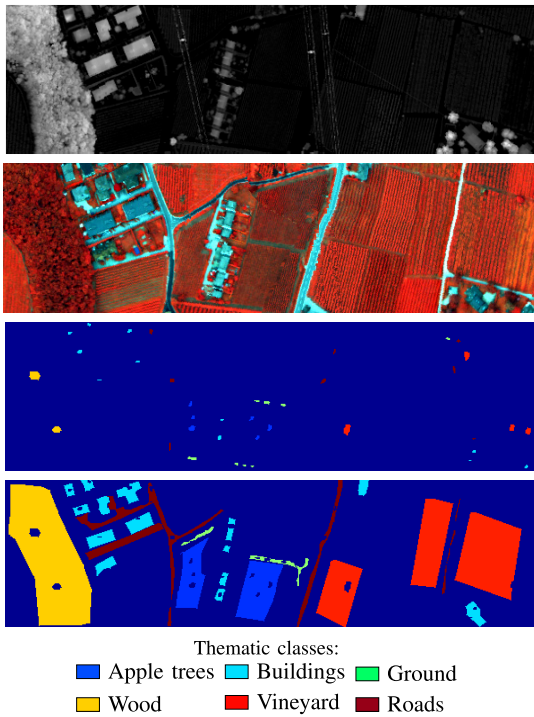


Fig. 3. Trento—from top to bottom: LiDAR-derived rasterized data set, a color composite representation of the HSI using bands 40, 20, and 10, as R, G, and B, respectively, training samples; test samples, and legend of different classes.

TABLE II
TRENTO—NUMBER OF TRAINING AND TEST SAMPLES

Class		Number of Samples	
No	Name	Training	Test
1	Apple trees	129	3905
2	Buildings	125	2778
3	Ground	105	374
4	Wood	154	8969
5	Vineyard	184	10317
6	Roads	122	3252
Total		819	29595

B. Algorithm Setup

For the EPs, one only needs to define the number of desired levels (s) as the whole process is automatic. In this context,

in order to generate the EP for area, volume, and diagonal of the bounding box, the threshold values used to generate the profile are automatically given by $[3^j]$, where $j = 0, 1, \dots, s - 1$. The size of the EPs is $2s + 1$, since the original image should also be included in the profile. The profiles have been computed using the four-connected connectivity rule. Here, s is set to seven, as suggested in [23].

SLRCA is initialized as suggested in [35]. The tuning parameter λ indicates the level of smoothness. In the experiments, λ is set to one percent of the intensity range of the extracted features. A fast wavelet toolbox provided in [46] was used for the implementation of Wavelet transforms. Daubechies wavelet with two coefficients and five decomposition levels is used in all the experiments.

In terms of the SVM, a radial basis function (RBF) kernel is used. The optimal hyperplane parameters C (parameter that controls the amount of penalty during the SVM optimization) and γ (spread of the RBF kernel) have been traced in the range of $C = 10^{-2}, 10^{-1}, \dots, 10^4$ and $\gamma = 10^{-3}, 10^{-2}, \dots, 10^4$ using fivefold cross validation.

For the RF, the number of trees is set to 300. The number of the prediction variable is set approximately to the square root of the number of input bands.

For the sake of simplicity, the following names are used in the experimental part: **LiDAR** and **HSI** show the classification accuracies of the LiDAR-derived DSM and HSI, respectively. **EP_{LiDAR}** and **EP_{HSI}** show the classification accuracies of EPs applied to LiDAR and HSI. **EP_{LiDAR+HSI}** refers to the classification accuracies of EPs applied to the stack of LiDAR and HSI.

C. Classification Experiments

1) *Classification Accuracies With Respect to the Number of Features*: Parameter r gives the number of fused features estimated by the proposed algorithm. Therefore, it is of interest to see the performance of the fusion algorithm with respect to the number of features selected. To do so, the standard training and test samples given in Tables I and II are used in this section. Fig. 4(a) and (b) demonstrates the OA in percentage with respect to r for Houston and Trento data sets. The simulations are given for $5 \leq r \leq 80$ for every five features increment and for both RF and SVM classifiers. As it can be seen in Fig. 4(a), for Houston, RF gives OA over 90% for $r \geq 35$ and OA for SVM gradually increases by r and goes over 90% when using more than 70 features.

In the case of the Trento data set [Fig. 4(b)], for $r \geq 15$, the OA is around 99% (the minimum OA is 98.95% for $r = 15$ and the maximum OA is 99.37 for $r = 20$) and for SVM is around 98% (the minimum OA is 97.78% for $r = 40$ and the maximum OA is 98.35% for $r = 15$).

Note that RF classifier considerably outperforms SVM based on OA when using higher features ($r > 10$), while for fewer features ($r = 5$ and $r = 10$), SVM performs better especially in the case of Trento data set.

The simulations in this section show that the SLRCA fusion technique by fusing the EP-derived features applied to LiDAR and HSI is able to provide high classification accuracies

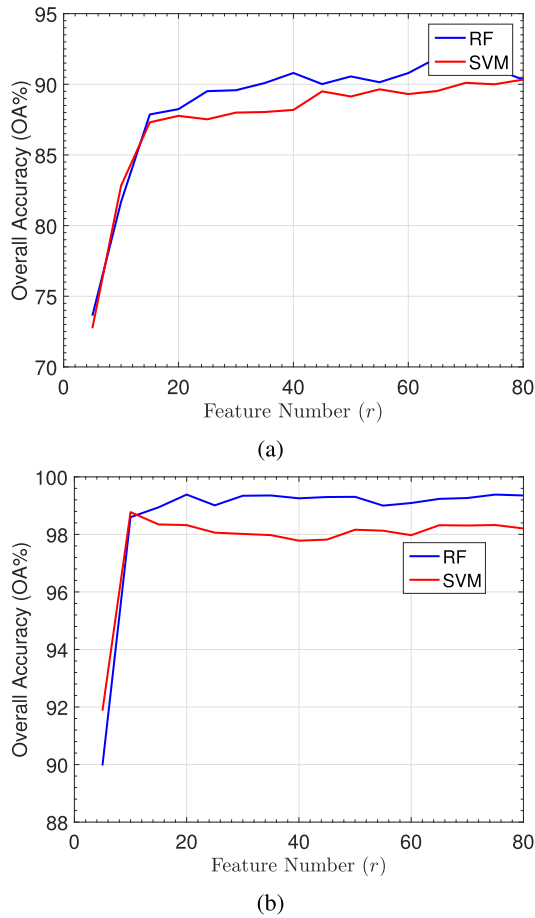


Fig. 4. Performance of OA with respect to feature number r obtained by applying RF and SVM classifiers on the fused features estimated by SLRCA from the (a) University of Houston data set (b) Trento data set.

using fewer fused features. However, for the proposed method, we suggest the number of fused features to be automatically set to the minimum number of the features in **HSI**, **EP_{HSI}**, and **EP_{LiDAR}**. In this context, for the Houston data, this value is set to 71 (i.e., the minimum value among 144 features of **HSI**, 213 features of **EP_{HSI}**, and 71 features of **EP_{LiDAR}**), while for the Trento data, this value is set to 63 (i.e., the minimum value among 63 features of **HSI**, 213 features of **EP_{HSI}**, and 71 features of **EP_{LiDAR}**).

2) *Classification Accuracies With Respect to the Number of Training Samples*: In this section, the performance of the proposed fusion technique is investigated in terms of the number of training samples selected for the classification task based on the OA. Here, the number of features selected for the Houston data set is 71 and for the Trento data set is 63 as explained in Section III-C1. Fig. 5(a) and (b) depicts the OAs obtained by RF and SVM using 5, 10, 25, and 50 samples per class for the classification of Houston and Trento data sets, respectively. Here, the results shown are the mean values of 20 times selecting the training samples randomly and the standard deviations were shown by the error bars. As can be seen from Fig. 5(a) and (b), the trends of the graphs are similar for both Houston and Trento data sets. The outcome of this experiment can be summarized as follows.

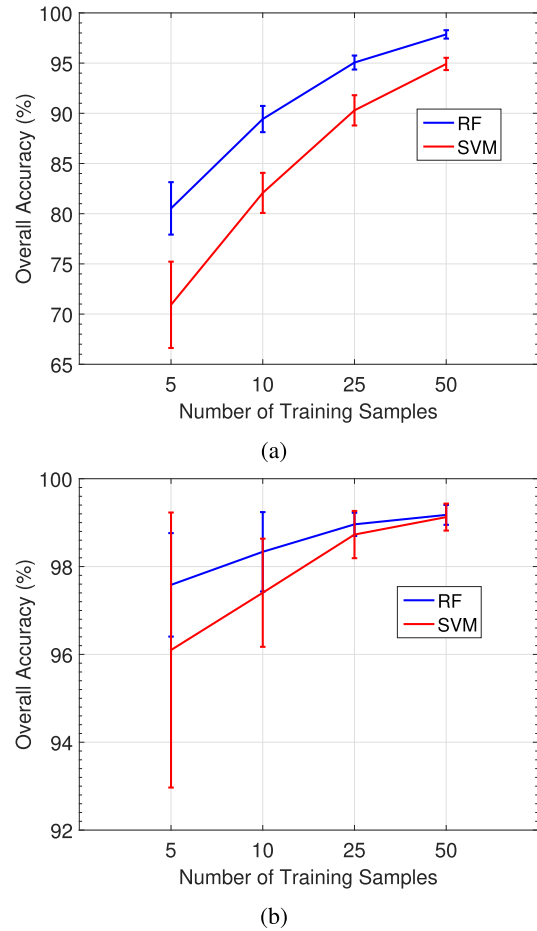


Fig. 5. Performance of OA with respect to the number of training samples obtained by applying RF and SVM classifiers on the fused features estimated by SLRCA from the (a) University of Houston data set (b) Trento data set.

- 1) SLRCA fusion gives accurate classification results also in the case of having low training samples. For example, in the case of Houston and using RF, as can be seen from Fig. 5(a), the OA is 89.43% using only ten samples per class and it goes over 95% using 25 samples. Note that, using 50 training samples per class, SLRCA fusion provides very high accurate classification results where $OA = 97.86\%$. Also, SVM gives $OA = 90.30\%$ and 94.92% using 25 and 50 samples, respectively.
- 2) For both data sets and in all the cases, RF outperforms SVM. This confirms that RF is a better option as a classifier for the proposed technique.
- 3) Comparing the error bars for RF and SVM confirms the robustness of RF for the classification tasks. This fact is clearer in the case of selecting five samples for the classification task. Specifically, in the case of Trento and using five training samples per class, the SVM standard deviation is more than double of the RF one.
- 4) Classification accuracies obtained are higher in all cases for Trento data set compared with Houston, which is expected since data set was captured over a rural area and therefore, there exists less structure and detail in the scene (and consequently fewer class of interests). For Trento, using RF, OA starts from 97.58% at five samples and goes up to 99.18% at 50 samples and using

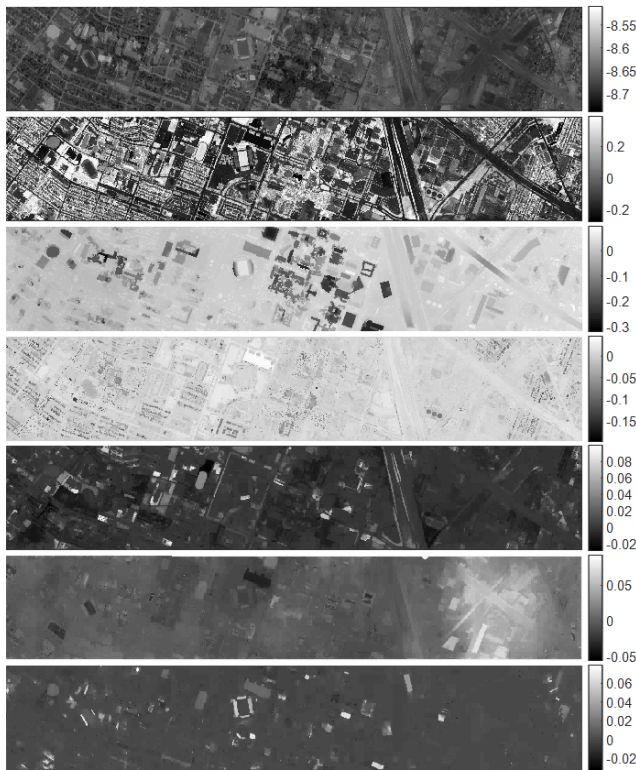


Fig. 6. Fused features estimated by applying SLRCA on EPs obtained from HSI and LiDAR of Houston data set. From top to bottom, the numbers of features are 1, 3, 6, 13, 20, 30, and 60.

SVM, OA starts from 96.10% at five samples and goes up to 99.13% at 50 samples.

3) *Estimated Fused Features*: The fused features estimated by applying the SLRCA fusion are shown in Fig. 6 for the Houston data set. From top to bottom, the numbers of features are 1, 3, 6, 13, 20, 30, and 60. As can be seen from Fig. 6, features with lower numbers are more informative visually compared with the ones with higher numbers, which is due to the tendency of SLRCA to find a low-rank representation for the high-dimensional features. This can also be seen in Fig. 4, where OAs reach to quiet high values using only a few features.

4) *SLRCA Fusion Compared With Other Techniques*: Here, the proposed fusion technique is compared with other techniques based on the classification accuracies. The classification results are given in Table III for the Houston data set and Table IV for the Trento data set. The results are compared based on class accuracies, OA, AA, and kappa coefficient (κ). The numbers of features used for the classification task in each case are given in the brackets.

As can be seen from Table III, the consideration of the spatial information extracted by the EP can considerably improve classification accuracies compared with the situations where the SVM and RF have directly been applied to the input data sets. For example, EPs on the LiDAR data (with 71 features) substantially improve the OA of **LiDAR** by almost 42% for the RF classifier. In the case of the HSI, due to the rich spectral information, the consideration of the EPs slightly improves the OA by almost 1% and 3%, using SVM and RF, respectively. **LiDAR + HSI** outperform

the individual use of each data, which confirms that HSI and LiDAR provide complement information to distinguish different classes of interest. In contrast, the integration of EPs for HSI and LiDAR decreases the OA by almost 1.5%, which confirms the drawbacks of high dimensionality on the classification task that can be more severe for the higher number of classes. It can also be seen that, by integrating HSI with EPs for HSI and LiDAR, the accuracies obtained by SVM have not been changed while the ones obtained by RF have been slightly improved. The SLRCA fusion method clearly captures the redundant information existing in the HSI and LiDAR profiles and leads to the accuracy of over 91%, which is the best classification accuracy among all the approaches considered in this paper for SVM. Note that the number of features used in the case of SLRCA fusion is 25% of the integration of the profiles.

A similar trend can be seen in the case of using RF, with a difference that the high dimensionality of the EPs does not affect the performance of the RF classifier and as can be seen the integration of HSI and LiDAR profiles improves OA by over 6%. However, SLRCA fusion improves the OA by more than 4% using 75% less features.

As can be seen from Table IV, in the case of the Trento data set, the use of the EP can considerably improve classification accuracies due to the fact that the EP can effectively extract spatial and contextual information. In addition, for the RF classifier, the 63 fused features obtained by applying OTVCA improve the classification accuracies compared with the integrated profiles (284 features) and for SVM the classification accuracies obtained are slightly less than the integrated profiles.

Overall, Tables III and IV show that the SLRCA fusion improves the classification accuracies using fewer number of features for both rural and urban data sets. Moreover, from Tables III and IV, it can be seen that the RF provides higher OA, AA, and kappa coefficients than the SVM.

The classification maps obtained by applying RF and SVM on **HSI**, **LiDAR + HSI**, and the fused features using SLRCA are shown in Figs. 7 and 8 for Houston and Trento data sets, respectively. It can be seen that the proposed fusion technique provides classification maps having homogeneous regions while preserving the structures, which is greatly of the interest specifically in the case of urban data sets. This is because of using spatial filtering obtained by the sparsity penalty on the sparse wavelet coefficients.

D. Comparison With Other Techniques in the Literature

In this section, the proposed approach is compared with the state of the art based on the classification accuracies. In the case of Trento data set, the proposed technique outperforms the ones published in [47] and [16] in terms of classification accuracies for both SVM and RF. This improvement might be due to the use of EPs instead of APs in the proposed approach.

In the case of Houston data set, compared with the 2013 Fusion Contest,² SLRCA fusion gives competitive classification accuracies. Note that the classification techniques partic-

²<http://www.grss-ieee.org/community/technical-committees/data-fusion/2013-ieee-grss-data-fusion-classification-contest-results/>



Fig. 7. Classification maps for Houston data. (a) Outputs of RF on HSI. (b) Output of SVM on HSI. (c) Output of RF on LiDAR + HSI. (d) Outputs of SVM on LiDAR + HSI. (e) Output of the proposed method using RF. (f) Output of the proposed method using SVM.

TABLE III

HOUSTON—CLASSIFICATION ACCURACIES OBTAINED BY DIFFERENT APPROACHES USING RF AND SVM. THE METRICS AA AND OA ARE REPORTED IN PERCENTAGE. KAPPA COEFFICIENT IS OF NO UNITS. THE BEST RESULT IS SHOWN IN BOLD. THE NUMBER OF FEATURES ARE WRITTEN IN PARENTHESES

	LiDAR (1)		HSI (144)		EP _{LiDAR} (71)		EP _{HSI} (213)		LiDAR+HSI (145)		EP _{LiDAR+HSI} (284)		EP _{LiDAR+HSI} + HSI(414)		SLRCA fusion (71)	
	SVM	RF	SVM	RF	SVM	RF	SVM	RF	SVM	RF	SVM	RF	SVM	RF	SVM	RF
OA	28.82	31.83	84.69	77.47	67.2	73.42	85.82	80.36	88.43	80.50	86.87	86.98	86.43	88.14	91.21	91.30
AA	36.31	37.43	86.34	80.34	70.00	75.97	83.08	83.47	89.64	82.84	88.78	88.54	88.46	89.52	90.09	91.95
K	0.2422	0.2677	0.8340	0.7563	0.6440	0.7120	0.8168	0.7876	0.8745	0.7887	0.8577	0.8592	0.8531	0.8717	0.8924	0.9056
1	11.68	13.49	83.48	83.38	57.36	74.26	79.39	77.49	83.00	83.57	79.39	78.06	79.58	81.96	80.06	81.58
2	0.00	16.26	96.43	98.40	40.79	61.75	78.85	78.48	97.84	98.12	80.36	84.96	81.39	97.93	94.74	99.44
3	87.13	56.63	99.80	98.02	98.61	97.23	100.00	100.00	99.80	98.42	100.00	100.00	100.00	100.00	100.00	98.61
4	51.80	44.03	98.77	97.54	92.33	58.14	87.78	82.77	98.96	97.82	95.83	95.45	96.12	98.86	96.88	96.12
5	12.12	58.05	98.11	96.40	83.43	82.10	99.81	97.73	98.48	96.40	99.81	98.77	98.11	94.41	99.05	99.72
6	78.32	58.04	95.10	97.20	78.32	83.22	95.80	95.80	99.30	95.80	95.80	95.80	95.80	95.80	95.80	98.60
7	56.90	39.09	89.09	82.09	55.22	77.33	85.17	73.23	87.41	84.61	80.41	73.41	74.63	74.25	85.73	90.39
8	13.11	29.53	45.87	40.65	29.06	68.28	65.15	59.92	70.94	57.74	90.41	85.28	88.89	88.60	86.42	95.73
9	14.92	13.60	82.53	69.78	67.33	59.40	89.90	83.00	86.69	70.35	89.80	93.96	80.17	86.12	86.02	98.21
10	8.30	11.29	83.20	57.63	61.39	66.89	51.54	64.09	82.53	56.95	56.66	67.08	72.68	67.08	66.99	63.42
11	72.68	40.42	83.87	76.09	99.72	99.91	87.76	84.72	89.94	79.98	90.70	90.89	88.61	91.46	98.29	90.70
12	0.00	9.99	70.99	49.38	63.11	64.75	84.34	78.10	78.19	59.65	89.91	88.57	88.57	88.38	96.35	91.07
13	12.28	15.09	70.53	61.40	49.12	58.60	84.56	77.89	72.98	65.26	84.56	76.14	84.21	77.89	81.75	76.49
14	97.57	80.16	100.00	99.60	100.00	100.00	100.00	99.60	100.00	100.00	100.00	100.00	100.00	100.00	100.00	100.00
15	27.91	75.90	97.46	97.67	74.21	87.74	97.25	99.37	98.52	97.89	98.10	99.79	98.10	100.00	100.00	99.15

TABLE IV

TRENTO—CLASSIFICATION ACCURACIES OBTAINED BY DIFFERENT APPROACHES USING RF AND SVM. THE METRICS AA AND OA ARE REPORTED IN PERCENTAGE. KAPPA COEFFICIENT IS OF NO UNITS. THE BEST RESULT IS SHOWN IN BOLD. THE NUMBER OF FEATURES ARE WRITTEN IN PARENTHESES

	LiDAR (1)		HSI (63)		EP _{LiDAR} (71)		EP _{HSI} (213)		LiDAR+HSI (64)		EP _{LiDAR+HSI} (284)		EP _{LiDAR+HSI} + HSI(347)		SLRCA fusion (63)	
	SVM	RF	SVM	RF	SVM	RF	SVM	RF	SVM	RF	SVM	RF	SVM	RF	SVM	RF
OA	63.30	46.70	84.55	84.92	81.27	85.17	96.28	95.90	85.06	90.61	98.68	98.39	98.77	98.98	98.13	99.27
AA	46.14	43.31	85.14	85.01	82.50	84.43	93.89	93.53	88.70	89.17	97.79	97.06	97.08	97.65	97.45	98.55
K	0.5039	0.3350	0.7965	0.8004	0.7637	0.8099	0.9505	0.9453	0.8068	0.8566	0.9824	0.9785	0.9835	0.9863	0.9751	0.9902
1	37.10	42.50	88.40	86.20	98.56	96.06	99.93	97.82	91.27	86.09	99.95	97.62	99.62	100.00	100.00	99.87
2	41.40	51.30	82.60	85.90	96.21	98.42	97.97	94.25	95.83	93.87	97.24	96.80	96.51	97.48	97.37	98.74
3	0.00	34.20	97.60	96.80	70.15	72.03	97.08	94.99	91.65	97.91	96.45	94.36	92.25	94.92	94.92	97.33
4	67.40	52.60	96.90	95.70	98.64	99.45	99.81	99.22	98.48	97.05	99.57	99.97	99.79	99.99	99.99	100.00
5	87.60	46.50	77.10	80.10	58.39	69.89	99.57	98.76	66.82	82.76	99.26	99.10	99.61	99.84	96.90	99.67
6	79.90	32.40	67.90	65.00	73.06	70.79	69.03	76.15	88.19	86.01	94.27	94.55	94.72	93.64	95.54	95.68

ipated in the contest had been specifically developed for the Houston data and they include several overheads, preprocessing and postprocessing approaches for further classification

improvements. In this paper, we have tried to propose a scheme, which is also applicable to other data sets composing of coregistered HSI and LiDAR by preserving the generaliza-

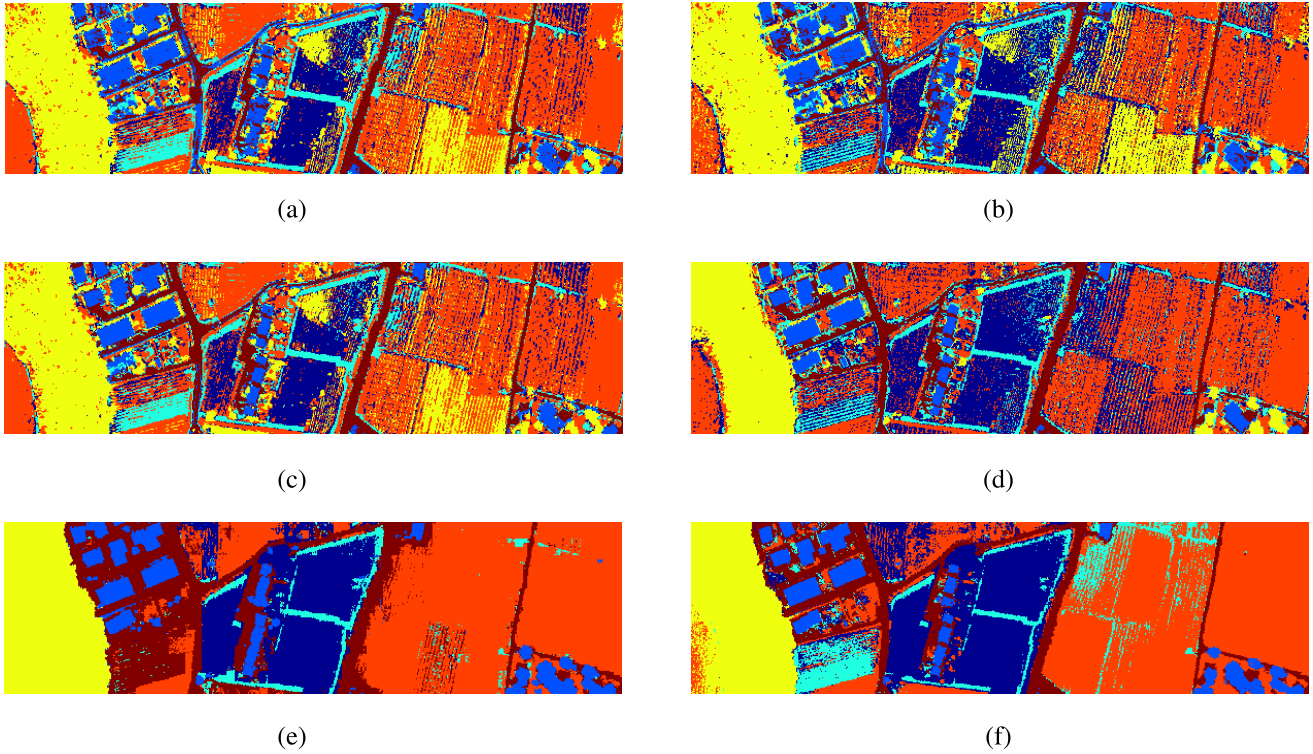


Fig. 8. Classification maps for Houston data. (a) Outputs of RF on **HSI**. (b) Output of SVM on **HSI**. (c) Output of RF on **LiDAR + HSI**. (d) Outputs of SVM on **LiDAR + HSI**. (e) Output of the proposed method using RF. (f) Output of the proposed method using SVM.

tion capability of the proposed approach, while achieving the highest classification accuracy on one specific data set is not expected.

Also, SLRCA fusion outperforms the fusion technique given in [2] for the Houston data set, when no postprocessing is applied. Even when Markov random field (MRF) is used for postprocessing in [2], the classification results obtained by SRLCA fusion are still competitive. However, the considerable improvements obtained in [2] using the postprocessing step have encouraged us to examine the effect of the hidden MRF proposed in [48] to further improve the classification accuracy of the proposed approach in future.

IV. CONCLUSION

In this paper, a new technique for the fusion of hyperspectral and LiDAR data was proposed called SLRCA fusion. The fusion methodology consists of two main phases. At phase I, spatial and elevation information from hyperspectral and LiDAR data sets is extracted using EPs. At phase II, the SLRCA fusion utilizes an SLRCA to fuse extracted features. The resulting fused features are of lower dimension than the profiles.

For the experiments, Houston (urban) and Trento (rural) data sets have been used. Both RF and SVM classifiers were used to perform the classification task. It has been shown that applying EPs considerably improves the classification accuracies due to effectively extract spatial and contextual information. The integration of LiDAR and HSI profiles increases the dimensionality, and as shown in the experiments, might not successfully improve the classification accuracies due to the Hughes phenomenon. Therefore, SLRCA fusion

was used to decrease the dimensionality by fusing the LiDAR and HSI profiles while preserving extracted information.

The experimental results revealed that applying SLRCA fusion improves the classification accuracies compared with the integrated profiles using low-dimensional fused features. In other words, SLRCA fusion is able to capture the redundancy of the features while improves the classification accuracies. This has been shown based on the classification accuracies obtained using both RF and SVM classifiers for both rural and urban data sets. Furthermore, RF has demonstrated to be well suited for the classification of the features obtained by the proposed approach.

In addition, it has been shown that the low-dimensional fused features obtained by applying SLRCA fusion provide accurate classification results in the case of selecting few training samples. Finally, the experiments confirm that SLRCA fusion is well competitive with other fusion techniques in the literature, which also exploit preprocessing and postprocessing techniques.

APPENDIX 2-D WAVELET TRANSFORM

The 2-D wavelet transform (shown by matrix **D**) we use is separable in the sense that first 1-D wavelet transform is applied on the rows of the image and then on the columns (separable bases). Assuming 2-D image **X**, applying 2-D wavelet transform (WT_{2-D}) can be written as

$$WT_{2-D}(\mathbf{X}) = \mathbf{D}_{1D}\mathbf{X}\mathbf{D}_{1D}^T \quad (12)$$

where \mathbf{D}_{1D} is a matrix that contains the 1-D wavelet bases in its columns. If we vectorize this expression, we get

$$\text{vec}(\mathbf{D}_{1D}\mathbf{X}\mathbf{D}_{1D}^T) = \mathbf{D}\mathbf{x} \quad (13)$$

where $\mathbf{D} = \mathbf{D}_{1D} \otimes \mathbf{D}_{1D}$ and $\mathbf{x} = \text{vec}(\mathbf{X})$ [49]. We can go from (12) to (13) and vice versa, and therefore no spatial information is lost.

ACKNOWLEDGMENT

The authors would like to thank Prof. L. Bruzzone of the University of Trento for providing the Trento data set, National Center for Airborne Laser Mapping (NCALM) at the University of Houston for providing the Houston data set, and the IEEE GRSS Image Analysis and Data Fusion Technical Committee for organizing the 2013 Data Fusion Contest, and Prof. N. Yokoya for providing the shadow-removed hyperspectral data.

REFERENCES

- [1] C. Debes *et al.*, "Hyperspectral and LiDAR data fusion: Outcome of the 2013 GRSS data fusion contest," *IEEE J. Sel. Topics Appl. Earth Observ. Remote Sens.*, vol. 7, no. 6, pp. 2405–2418, Jun. 2014.
- [2] M. Khodadadzadeh, J. Li, S. Prasad, and A. Plaza, "Fusion of hyperspectral and LiDAR remote sensing data using multiple feature learning," *IEEE J. Sel. Topics Appl. Earth Observ. Remote Sens.*, vol. 8, no. 6, pp. 2971–2983, Jun. 2015.
- [3] P. Gamba, F. Dell'Acqua, and B. V. Dasarathy, "Urban remote sensing using multiple data sets: Past, present, and future," *IEEE Trans. Geosci. Remote Sens.*, vol. 6, no. 4, pp. 319–326, Dec. 2005.
- [4] J. Plaza, A. Plaza, P. Gamba, and G. Trianni, "Efficient multi-band texture analysis for remotely sensed data interpretation in urban areas," in *Proc. IEEE Urban Remote Sens. Joint Event*, Apr. 2007, pp. 1–6.
- [5] Q. Chen, "Airborne LiDAR data processing and information extraction," *Photogramm. Eng. Remote Sens.*, vol. 73, no. 2, pp. 109–112, 2007.
- [6] B. Höfle, M. Hollaus, and J. Hagenauer, "Urban vegetation detection using radiometrically calibrated small-footprint full-waveform airborne LiDAR data," *ISPRS J. Photogramm. Remote Sens.*, vol. 67, pp. 134–147, Jan. 2012.
- [7] G. P. Asner *et al.*, "Invasive species detection in hawaiian rainforests using airborne imaging spectroscopy and LiDAR," *Remote Sens. Environ.*, vol. 112, no. 5, pp. 1942–1955, 2008.
- [8] G. A. Blackburn, "Remote sensing of forest pigments using airborne imaging spectrometer and LiDAR imagery," *Remote Sens. Environ.*, vol. 82, nos. 2–3, pp. 311–321, 2002.
- [9] M. Voss and R. Sugumaran, "Seasonal effect on tree species classification in an urban environment using hyperspectral data, LiDAR, and an object-oriented approach," *Sensors*, vol. 8, no. 5, pp. 3020–3036, 2008.
- [10] R. M. Lucas, A. C. Lee, and P. J. Bunting, "Retrieving forest biomass through integration of CASI and LiDAR data," *Int. J. Remote Sens.*, vol. 29, no. 5, pp. 1553–1577, 2008.
- [11] U. Heiden, W. Heldens, S. Roessner, K. Segl, T. Esch, and A. Mueller, "Urban structure type characterization using hyperspectral remote sensing and height information," *Landscape Urban Planning*, vol. 105, no. 6, pp. 361–375, Jun. 2012.
- [12] R. K. Hall, R. L. Watkins, D. T. Heggem, K. B. Jones, P. R. Kaufmann, and S. B. Moore, "Quantifying structural physical habitat attributes using LiDAR and hyperspectral imagery," *Environ. Monitor. Assessment*, vol. 159, nos. 1–4, pp. 63–83, 2009.
- [13] B. Koetz, F. Morsdorf, S. van der Linden, T. Curt, and B. Allgöwer, "Multi-source land cover classification for forest fire management based on imaging spectrometry and LiDAR data," *Forest Ecol. Manag.*, vol. 256, no. 3, pp. 263–271, 2008.
- [14] J. T. Mundt, D. R. Streutker, and N. F. Glenn, "Mapping sagebrush distribution using fusion of hyperspectral and LiDAR classifications," *Photogramm. Eng. Remote Sens.*, vol. 72, no. 1, pp. 47–54, Sep. 2006.
- [15] R. Sugumaran and M. Voss, "Object-oriented classification of LiDAR-fused hyperspectral imagery for tree species identification in an urban environment," in *Proc. Urban Remote Sens. Joint Event*, Apr. 2007, pp. 1–6.
- [16] P. Ghamisi, J. A. Benediktsson, and S. Phinn, "Land-cover classification using both hyperspectral and LiDAR data," *Int. J. Image Data Fusion*, vol. 6, no. 3, pp. 189–215, 2015.
- [17] M. Dalponte, L. Bruzzone, and D. Gianelle, "Fusion of hyperspectral and lidar remote sensing data for classification of complex forest areas," *IEEE Trans. Geosci. Remote Sens.*, vol. 46, no. 5, pp. 1416–1427, May 2008.
- [18] W. Liao, A. Pižurica, R. Bellens, S. Gautama, and W. Philips, "Generalized graph-based fusion of hyperspectral and LiDAR data using morphological features," *IEEE Geosci. Remote Sens. Lett.*, vol. 12, no. 3, pp. 552–556, Mar. 2015.
- [19] P. Ghamisi, B. Höfle, and X. X. Zhu, "Hyperspectral and LiDAR data fusion using extinction profiles and deep convolutional neural network," *IEEE J. Sel. Topics Appl. Earth Observ. Remote Sens.*, vol. 10, no. 6, pp. 3011–3024, Jun. 2017.
- [20] T. Matsuki, N. Yokoya, and A. Iwasaki, "Hyperspectral tree species classification of japanese complex mixed forest with the aid of LiDAR data," *IEEE J. Sel. Topics Appl. Earth Observ. Remote Sens.*, vol. 8, no. 5, pp. 2177–2187, May 2015.
- [21] B. Rasti, P. Ghamisi, and R. Gloaguen, "Hyperspectral and lidar fusion using extinction profiles and total variation component analysis," *IEEE Trans. Geosci. Remote Sens.*, vol. 55, no. 7, pp. 3997–4007, Jul. 2017.
- [22] P. Ghamisi, R. Souza, J. A. Benediktsson, X. X. Zhu, L. Rittner, and R. Lotufo, "Extinction profiles for the classification of remote sensing data," *IEEE Trans. Geosci. Remote Sens.*, vol. 54, no. 10, pp. 5631–5645, Oct. 2016.
- [23] P. Ghamisi, R. Souza, J. A. Benediktsson, L. Rittner, R. Lotufo, and X. X. Zhu, "Hyperspectral data classification using extended extinction profiles," *IEEE Geosci. Remote Sens. Lett.*, vol. 13, no. 11, pp. 1641–1645, Nov. 2016.
- [24] P. Ghamisi, M. D. Mura, and J. A. Benediktsson, "A survey on spectral-spatial classification techniques based on attribute profiles," *IEEE Trans. Geosci. Remote Sens.*, vol. 53, no. 5, pp. 2335–2353, May 2015.
- [25] J. A. Benediktsson and P. Ghamisi, *Spectral-Spatial Classification of Hyperspectral Remote Sensing Images*. Boston, MA, USA: Artech House, 2015.
- [26] M. D. Mura, J. A. Benediktsson, B. Waske, and L. Bruzzone, "Morphological attribute profiles for the analysis of very high resolution images," *IEEE Trans. Geosci. Remote Sens.*, vol. 48, no. 10, pp. 3747–3762, Oct. 2010.
- [27] G. Hughes, "On the mean accuracy of statistical pattern recognizers," *IEEE Trans. Inf. Theory*, vol. 14, no. 1, pp. 55–63, Jan. 1968.
- [28] P. Ghamisi, "Spectral and spatial classification of hyperspectral data," Ph.D. dissertation, Dept. Elect. Comput. Eng., Univ. Iceland, Reykjavik, Iceland, 2015.
- [29] P. Ghamisi and J. A. Benediktsson, "Feature selection based on hybridization of genetic algorithm and particle swarm optimization," *IEEE Geosci. Remote Sens. Lett.*, vol. 12, no. 2, pp. 309–313, Feb. 2015.
- [30] P. Ghamisi, M. S. Couceiro, and J. A. Benediktsson, "A novel feature selection approach based on FODPSO and SVM," *IEEE Trans. Geosci. Remote Sens.*, vol. 53, no. 5, pp. 2935–2947, May 2015.
- [31] Y. Bazi and F. Melgani, "Toward an optimal SVM classification system for hyperspectral remote sensing images," *IEEE Trans. Geosci. Remote Sens.*, vol. 44, no. 11, pp. 3374–3385, Nov. 2006.
- [32] B. Rasti, J. R. Sveinsson, M. O. Ulfarsson, and J. A. Benediktsson, "Hyperspectral image denoising using a new linear model and sparse regularization," in *Proc. IEEE Int. Geosci. Remote Sens. Symp. (IGARSS)*, Jul. 2013, pp. 457–460.
- [33] J. M. Bioucas-Dias *et al.*, "Hyperspectral unmixing overview: Geometrical, statistical, and sparse regression-based approaches," *IEEE J. Sel. Topics Appl. Earth Observ. Remote Sens.*, vol. 5, no. 2, pp. 354–379, Apr. 2012.
- [34] B. Rasti, "Sparse hyperspectral image modeling and restoration," Ph.D. dissertation, Dept. Elect. Comput. Eng., Univ. Iceland, Reykjavik, Iceland, Dec. 2014.
- [35] B. Rasti, J. R. Sveinsson, and M. O. Ulfarsson, "Wavelet-based sparse reduced-rank regression for hyperspectral image restoration," *IEEE Trans. Geosci. Remote Sens.*, vol. 52, no. 10, pp. 6688–6698, Oct. 2014.
- [36] C. Vachier, "Extinction value: A new measurement of persistence," in *Proc. IEEE Workshop Nonlinear Signal Image Process.*, vol. 1, Jul. 1995, pp. 254–257.
- [37] E. J. Breen and R. Jones, "Attribute openings, thinnings, and granulometries," *Comput. Vis. Image Understand.*, vol. 64, no. 3, pp. 377–389, 1996.
- [38] A. G. Silva and R. de A. Lotufo, "New extinction values from efficient construction and analysis of extended attribute component tree," in *Proc. SIBGRAPI*, Oct. 2008, pp. 204–211.
- [39] P. Soille, "Morphological image analysis," in *Principles and Applications*, 2nd ed. New York, NJ, USA: Springer-Verlag, 2003.
- [40] R. Souza, L. Rittner, R. Machado, and R. Lotufo, "A comparison between extinction filters and attribute filters," in *Proc. ISMM*, 2015, pp. 63–74.

- [41] Y. Xu, T. Géraud, and L. Najman, "Morphological filtering in shape spaces: Applications using tree-based image representations," *CoRR*, Apr. 2012, pp. 485–488.
- [42] W. Liao, R. Bellens, S. Gautama, and W. Philips, "Feature fusion of hyperspectral and LiDAR data for classification of remote sensing data from urban area," in *Proc. 5th Workshop EARSeL Special Interest Group Land Use Land Cover*, 2014, p. 34.
- [43] B. Schölkopf, A. Smola, and K. Müller, "Nonlinear component analysis as a kernel eigenvalue problem," *Neural Comput.*, vol. 10, no. 5, pp. 1299–1319, 1998.
- [44] B. Rasti and K. S. Gudmundsson, "Sparse and low-rank feature extraction for the classification of target's tracking capability," *Proc. SPIE*, vol. 9970, pp. 99701U–1–99701U–7, Sep. 2016. [Online]. Available: <http://dx.doi.org/10.1117/12.2240282>
- [45] H. Zou, T. Hastie, and R. Tibshirani, "Sparse principal component analysis," *J. Comput. Graph. Stat.*, vol. 15, no. 2, pp. 265–286, 2006.
- [46] B. Rasti. (May 2016). *Wavelab Fast*. [Online]. Available: https://www.researchgate.net/publication/303445667_Wavelab_fast
- [47] M. Pedergnana, P. R. Marpu, M. D. Mura, J. A. Benediktsson, and L. Bruzzone, "Classification of remote sensing optical and LiDAR data using extended attribute profiles," *IEEE J. Sel. Topics Signal Process.*, vol. 6, no. 7, pp. 856–865, Nov. 2012.
- [48] P. Ghamisi, J. A. Benediktsson, and M. O. Ulfarsson, "Spectral–spatial classification of hyperspectral images based on hidden Markov random fields," *IEEE Trans. Geosci. Remote Sens.*, vol. 52, no. 5, pp. 2565–2574, May 2014.
- [49] J. R. Magnus and H. Neudecker, *Matrix Differential Calculus With Applications in Statistics and Econometrics*, 3rd ed. Hoboken, NJ, USA: Wiley, Jan. 2007.



Behnood Rasti (S'12–M'14) received the B.Sc. and M.Sc. degrees in electrical and electronics engineering from the University of Guilan, Rasht, Iran, in 2006 and 2009, respectively, and the Ph.D. degree in electrical and computer engineering from the Department of Electrical and Computer Engineering, University of Iceland, Reykjavik, Iceland, in 2014.

From 2015 to 2016, he was a Post-Doctoral Researcher with the University of Iceland. In 2016, he joined the Keilir Institute of Technology, Reykjaneshbaer, Iceland, where he is currently an Instructor. His research interests include signal and image processing, hyperspectral image analysis, remote sensing data fusion, biomedical engineering, biomedical data analysis, control system, and robotics.



Pedram Ghamisi (S'12–M'15) received the B.Sc. degree in civil (survey) engineering from Islamic Azad University South Tehran Branch, Tehran, Iran, the M.Sc. degree (Hons.) in remote sensing from the K.N.Toosi University of Technology, Tehran, in 2012, and the Ph.D. degree in electrical and computer engineering from the University of Iceland, Reykjavik, Iceland, in 2015.

Between 2013 and 2014, he spent seven months at the School of Geography, Planning, and Environmental Management, University of Queensland, Brisbane, QLD, Australia. In 2015, he was a Post-Doctoral Research Fellow with the University of Iceland, the Technical University of Munich, Munich, Germany, and Heidelberg University, Heidelberg, Germany. He has been a Researcher with the German Aerospace Center, Remote Sensing Technology Institute, Weßling, Germany, since 2015. His research interests include remote sensing and image analysis, with a special focus on spectral and spatial techniques for hyperspectral image classification, multisensor data fusion, machine learning, and deep learning.

Dr. Ghamisi was a recipient of the Best Researcher Award for M.Sc. students at the K. N. Toosi University of Technology during 2010–2011. In 2013, he presented at the IEEE International Geoscience and Remote Sensing Symposium, Melbourne, and was a recipient of the IEEE Mikio Takagi Prize for winning the conference Student Paper Competition against almost 70 people. He was a recipient of the prestigious Alexander von Humboldt Fellowship in 2015. In 2016, he was selected as a Talented International Researcher by the Iran's National Elites Foundation. In 2017, he won the Data Fusion Contest 2017 organized by the Image Analysis and Data Fusion Technical Committee of the Geoscience and Remote Sensing Society. His model was the most accurate among more than 800 submissions.



Javier Plaza (M'09–SM'15) received the M.Sc. and Ph.D. degrees in computer engineering from the Hyperspectral Computing Laboratory, Department of Technology of Computers and Communications, University of Extremadura, Badajoz, Spain, in 2004 and 2008, respectively.

He is currently a member with the Hyperspectral Computing Laboratory, Department of Technology of Computers and Communications, University of Extremadura. He was a Guest Editor of two special issues on hyperspectral remote sensing for different journals. He has authored more than 140 publications, including 45 *JCR* journal papers, 10 book chapters, and 90 peer-reviewed conference proceeding papers. His research interests include hyperspectral data processing and parallel computing of remote sensing data.

Dr. Plaza was a recipient of the Outstanding Ph.D. Dissertation Award from the University of Extremadura in 2008, the Best Column Award of the IEEE SIGNAL PROCESSING MAGAZINE in 2015, the most highly cited paper in the *Journal of Parallel and Distributed Computing* (2005–2010), and the Best Paper Awards at the IEEE International Conference on Space Technology and the IEEE Symposium on Signal Processing and Information Technology. He is an Associate Editor of the IEEE GEOSCIENCE AND REMOTE SENSING LETTERS and the IEEE Remote Sensing Code Library.



Antonio Plaza (M'05–SM'07–F'15) received the M.Sc. and Ph.D. degrees in computer engineering from the Hyperspectral Computing Laboratory, Department of Technology of Computers and Communications, University of Extremadura, Badajoz, Spain, in 1999 and 2002, respectively.

He is currently the Head with the Hyperspectral Computing Laboratory, Department of Technology of Computers and Communications, University of Extremadura. He has authored more than 600 publications, including 197 *JCR* journal papers (over 140 in IEEE journals), 23 book chapters, and 285 peer-reviewed conference proceeding papers. He has reviewed more than 500 manuscripts for over 50 different journals. His research interests include hyperspectral data processing and parallel computing of remote sensing data.

Prof. Plaza was a member of the Editorial Board of the IEEE GEOSCIENCE AND REMOTE SENSING NEWSLETTER from 2011 to 2012 and the IEEE GEOSCIENCE AND REMOTE SENSING MAGAZINE in 2013. He was also a member of the Steering Committee of the IEEE JOURNAL OF SELECTED TOPICS IN APPLIED EARTH OBSERVATIONS AND REMOTE SENSING (JSTARS). He was a recipient of the most Highly Cited Paper Award in the *Journal of Parallel and Distributed Computing* during 2005–2010, the recognition of Best Reviewers for the IEEE GEOSCIENCE AND REMOTE SENSING LETTERS in 2009 and the IEEE TRANSACTIONS ON GEOSCIENCE AND REMOTE SENSING in 2010, the 2013 Best Paper Award of JSTARS, and the Best Column Award of the IEEE SIGNAL PROCESSING MAGAZINE in 2015. He was a recipient of the Best Paper Awards at the IEEE International Conference on Space Technology and the IEEE Symposium on Signal Processing and Information Technology. He was a Guest Editor of ten Special Issues on Hyperspectral Remote Sensing for different journals. He was an Associate Editor of the IEEE ACCESS and the IEEE TRANSACTIONS ON GEOSCIENCE AND REMOTE SENSING from 2007 to 2012. He was the Director of Education Activities for the IEEE Geoscience and Remote Sensing Society (GRSS) from 2011 to 2012. He was the President of the Spanish Chapter of the IEEE GRSS from 2012 to 2016. He is currently the Editor-in-Chief of the IEEE TRANSACTIONS ON GEOSCIENCE AND REMOTE SENSING journal.